Available online at www.sciencedirect.com
ScienceDirect
Tectonophysics 432 (2007) 37–50
TECTONOPHYSICS
www.elsevier.com/locate/tecto

Shallow architecture of the Wadi Araba fault (Dead Sea Transform) from high-resolution seismic investigations

Ch. Haberland [a,*], N. Maercklin [b,1], D. Kesten [b,2], T. Ryberg [b], Ch. Janssen [b], A. Agnon [c], M. Weber [a,b], A. Schulze [b], I. Qabbani [d], R. El-Kelani [e]

[a] *Institute for Geosciences, University of Potsdam, Potsdam, Germany*
[b] *GeoForschungsZentrum Potsdam, Potsdam, Germany*
[c] *Institute of Earth Sciences, Hebrew University, Jerusalem, Israel*
[d] *Natural Resources Authority, Amman, Jordan*
[e] *An-Najah University, Earth Sciences and Seismic Engineering Centre, Nablus, Palestine*

Received 4 May 2006; received in revised form 10 November 2006; accepted 2 December 2006
Available online 21 December 2006

Abstract

In a high-resolution small-scale seismic experiment we investigated the shallow structure of the Wadi Araba fault (WAF), the principal fault strand of the Dead Sea Transform System between the Gulf of Aqaba/Eilat and the Dead Sea. The experiment consisted of 8 sub-parallel 1 km long seismic lines crossing the WAF. The recording station spacing was 5 m and the source point distance was 20 m. The first break tomography yields insight into the fault structure down to a depth of about 200 m. The velocity structure varies from one section to the other which were 1 to 2 km apart, but destinct velocity variations along the fault are visible between several profiles. The reflection seismic images show positive flower structures and indications for different sedimentary layers at the two sides of the main fault. Often the superficial sedimentary layers are bent upward close to the WAF. Our results indicate that this section of the fault (at shallow depths) is characterized by a transpressional regime. We detected a 100 to 300 m wide heterogeneous zone of deformed and displaced material which, however, is not characterized by low seismic velocities at a larger scale. At greater depth the geophysical images indicate a blocked cross-fault structure. The structure revealed, fault cores not wider than 10 m, are consistent with scaling from wear mechanics and with the low loading to healing ratio anticipated for the fault.

Keywords: Dead Sea Transform; Reflection seismics; Shear zone; Tomography; Strike–slip fault

1. Introduction

Continental shear zones accommodate the relative lateral movements of lithospheric plates and are a major element of global tectonics (Wilson, 1965). In large continental shear zones networks of subparallel brittle faults develop at different scales. These systems often consist of a large number of individual faults which stretch over many hundreds of kilometers. With increasing slip it seems, that the fault complexity

* Corresponding author.
E-mail addresses: haber@geo.uni-potsdam.de (C. Haberland), nmaercklin@gmail.com (N. Maercklin), dagmar.kesten@rpf.bwl.de (D. Kesten), trond@gfz-potsdam.de (T. Ryberg), jans@gfz-potsdam.de (C. Janssen), amotz@cc.huji.ac.il (A. Agnon), mhw@geo.uni-potsdam.de (M. Weber), robert@gfz-potsdam.de (A. Schulze), radwan@najah.edu (R. El-Kelani).
[1] Now at: University of Naples, Naples, Italy.
[2] Now at: Geologisches Landesamt Baden Würtemberg, Germany.

0040-1951/$ - see front matter © 2006 Elsevier B.V. All rights reserved.
doi:10.1016/j.tecto.2006.12.006

decreases, and most of the long-term slip is accommodated by only a few through-going structures (main faults) (Stirling et al., 1996). The deformation related to these movements is accomplished by different modes depending on the rheological conditions at different depth levels.

In the deeper parts of the crust and the upper (lithospheric) mantle ductile shear deformation prevails. There is evidence for a great variety of how these deep decoupling zones are developed. Different studies suggest localized deformation in the lower crust and/or upper mantle (Wittlinger et al., 1998; Rümpker et al., 2003), broadly distributed (continuous) deformation, transition of the latter two, or listric faulting into a lower crustal sub-horizontal detachment (see also Ritter et al., 2004, and references within).

The upper parts of the crust are deforming in a brittle regime. At seismogenic depth, fault structures are expected to be simpler than at shallow depths because increasing pressure and temperature tend to suppress brittle branching and other sources of structural complexity (Ben-Zion and Sammis, 2003). At the Punchbowl fault, an ancient, large displacement fault of the San Andreas Fault (SAF) system exhumed from a depth of 2 to 4 km, Chester and Logan (1986) elaborated the "typical brittle fault structure" consisting of three major entities, namely a) the undeformed host rock, b) the damaged host rock, and c) the main gouge zone.

However, closer to the surface, the fault structure often becomes more complex and the "simple" model does not automatically apply. Here we expect weathered, often unconsolidated material which deforms differently. Furthermore, complexity of surface and shallow rupture is often associated with slip partitioning between pure strike–slip and dip–slip modes originating in a deep oblique–slip master fault (Bowman et al., 2003). Expressions of such complexities at the surface are the development of different fault strands, positive and negative flower structures, pull-apart basins, pressure ridges etc. (Harding and Lowell, 1979). Nevertheless, there are many observations (often based on geophysical evidence) of the "classical" brittle fault structure at recently active (or at least young) strike slip fault systems, even at the surface (e.g., Li et al., 1994, 1997; Schulz and Evans, 2000; Ben-Zion et al., 2003). The knowledge of the detailed structure of the fault zone contributes to issues like the evolutional stage of the fault zone or the predominant stress regime.

The Dead Sea Transform (DST) in the Middle East is a large transform system which is still active today. Revealing the structure of the DST at a wide range of scales was the main aim of the collaborative and interdisciplinary research effort DESERT (DEad SEa Rift Transect). Seismological investigation (Rümpker et al., 2003) and refraction, reflection seismic investigations and receiver function studies (DESERT Team, 2004; Mohsen et al., 2005; Mechie et al., 2005) revealed the transform structure at the crustal scale. With seismic scattering analysis (Maercklin et al., 2004) and the combination of seismic tomography and magnetotelluric investigations (Ritter et al., 2003; Maercklin et al., 2005) the upper crustal seismic structure in the direct vicinity of the Wadi Araba fault (WAF), the principal fault strand of the DST, was studied down to 4 km depth. A study of guided waves furthermore detected a waveguide presumably related to the WAF (Haberland et al., 2003).

Here we present a high-resolution seismic study focusing on the top most 500 meters of the WAF and its vicinity, which complements the investigations at the mesoscopic scale. The results of the different studies covering a wide range of scales will be combined to form, together with geological observations, an integrating picture.

2. Geological setting

The DST, stretching from the Red Sea to the Tauros–Zagros collision zone, is a conspicuous active shear zone that played as one of two examples for a continental transform in Wilson's (1965) classical paper. It forms the plate boundary between the Sinai microplate in the West and the Arabian Plate in the East (Fig. 1), and exhibits a total displacement of about 100 km within the last 20 Myr (e.g., Garfunkel, 1981). The recent slip rate is estimated between 1 and 10 mm/yr (Joffe and Garfunkel, 1987; Klinger et al., 2000). Todays seismicity along the WAF is moderate, and only 30 to 50 smaller magnitude earthquakes occur per year along this transform segment. However, several strong earthquakes reportedly hit the region in the last centuries (e.g., Marco et al., 1996; Zilberman et al., 2005).

The elongated structure of the rift-like DST is composed of a series of large basins (with the Dead Sea being the most prominent one), which are mainly attributed to dilatational jogs related to the left-lateral strike–slip motion. Also the formation of the Gulf of Aqaba/Eilat had been associated with pull apart structures (e.g., Garfunkel, 1981; Ben-Avraham, 1985). At the Aqaba segment of the DST (between the Gulf of Aqaba and the Dead Sea basin), the rift valley is further divided into a series of smaller sub-basins (ten Brink et al., 1999). The sediments of the Evrona playa basin just North of the Gulf of Aqaba formed by Plio-

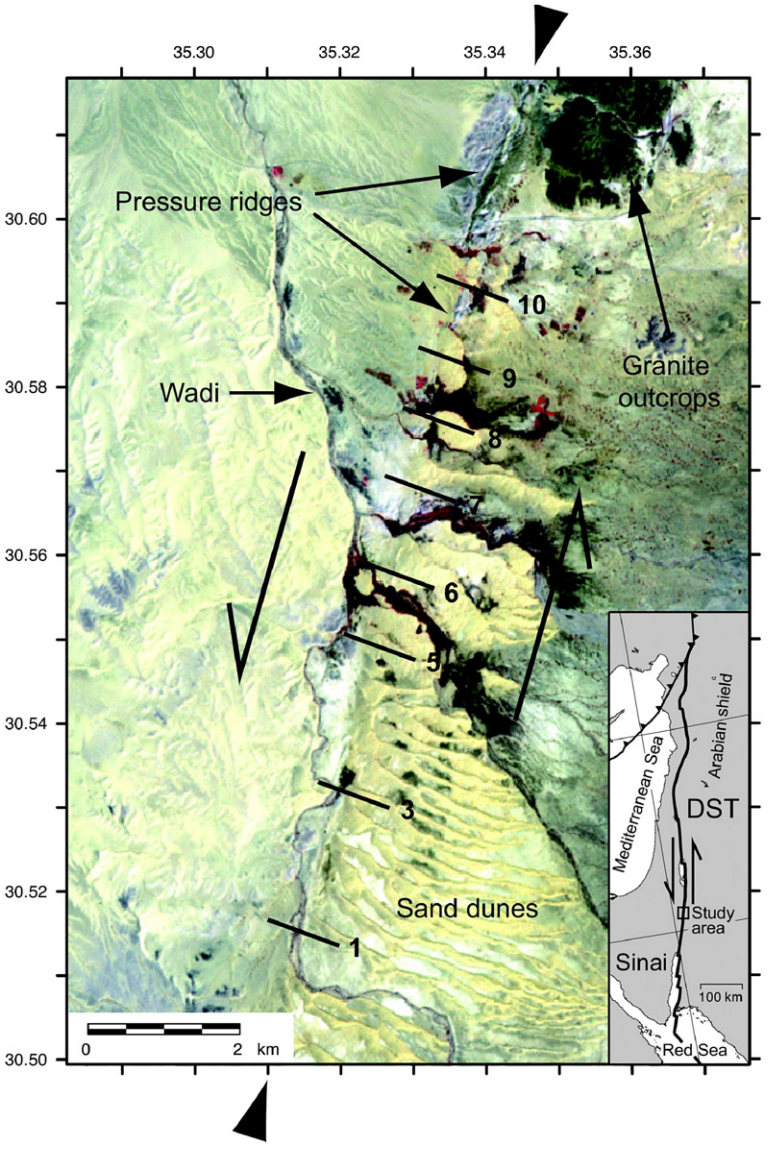

Fig. 1. Position of CSA-2 seismic lines overlayed on an ASTER satellite image of the study area. Large arrowheads mark the course of the Wadi Araba fault (WAF). The inset shows the principal geotectonic situation in the Middle East.

Pleistocene sand and silt, alternating with clay layers and gravel lenses, are crossed by the transform/strike–slip fault forming wide (1 km) flower structures (Shtivelman et al., 1998).

Commercial multichannel seismic reflection and drillhole data revealed the fault-bounded structure of the Dead Sea depression starting approximately 100 km North of the Gulf of Aqaba/Eilat. The data suggest an asymmetric, fullgraben geometry of flat sub-horizontal strata of Miocene to recent sediment fill shallowing toward the South (Zak and Freund, 1981; Ginzburg and Kashai, 1981; Kashai and Croker, 1987; ten Brink and Ben-Avraham, 1989; Rotstein et al., 1991; Garfunkel, 1997; Gardosh et al., 1997; Neev and Hall, 1997). The Miocene Hazeva formation is considered the oldest basin-fill unit, overlain by massive evaporite beds and sequences of marl, clay, sand, gravel (Zak, 1967; Gardosh et al., 1997; Garfunkel, 1997). A number of normal, often listric, faults dominate the structure in the southern Dead Sea basin (Gardosh et al., 1997).

Our study area is located in the eastern Araba valley just at the southern termination of the Dead Sea basin. The western side of this central portion of the Araba segment was intensely studied by high-resolution

seismic studies (Bartov et al., 1998; Frieslander, 2000). Several prominent faults cut the western half of the Araba valley, with the subvertical Zofar fault being the most prominent one. The northern part of the Zofar fault is interpreted as the western border-fault of the Dead Sea basin (Bartov et al., 1998), and besides an obvious normal fault character, a sinistral strike–slip component is assumed (Garfunkel, 1981). In the uppermost kilometer West of the Zofar fault, Cretaceous and Permian rocks are found, while younger strata related with the Dead Sea basin are exposed East of it (e.g., Ritter et al., 2003). Toward the center of the Araba valley there are indications of more North–South striking faults which often join at depth to form negative flower structures (Frieslander, 2000; Kesten et al., in press).

Several industrial seismic profiles and the DESERT NVR profile reveal the subsurface at the eastern side of the valley (Kesten, 2004; DESERT Team, 2004; Kesten et al., in press). Here, the Wadi Araba fault (WAF), which is considered to be the main active strike–slip fault strand of the DST, can be seen in the seismic images, however, with varying clarity. This characteristic might be related to the predominant strike–slip character. Indications of further near vertical faults and flower structures between Zofar fault and WAF are found on individual profiles. East of the WAF late Proterozoic igneous rocks, Cretaceous marine sediments and Paleozoic to early Cretaceous sandstones are exposed (Kesten et al., in press). More faults sub-parallel to the WAF are known at distances around 10 km to the East (Quaira fault) (Atallah, 1992; Kesten, 2004). Estimations for sinistral strike–slip at the Quaira fault varies from 8 to 40 km (e.g., Abu Taimeh, 1988; Barjus, 1988).

On satellite images it seems, that the WAF is represented by a single trace . The WAF trace is outlined by scarps, small rhomb-shaped grabens, pressure ridges (Fig. 2), and displaced alluvial fan toes indicating that strike–slip faulting is still active (Garfunkel et al., 1981; Ginat et al., 1998; Klinger et al., 2000; Niemi et al., 2001, and references within). The fault trends SSW–NNE, with a slight change in orientation by a few degrees eastward in the northern part of the area investigated (approximately at 30°36′ N, Fig. 1). This re-straining bend is clearly visible on satellite images and is responsible for the development of pressure ridges of Lower Cretaceous sandstones and Upper Cretaceous carbonates just north of 30 36′ N (Garfunkel et al., 1981; Barjous and Mikbel, 1990; Ginat et al., 1998; Kesten, 2004). The ridges, mostly exhumed fault zone rocks (Fig. 2), consist of steeply dipping beds of limestone and some fault breccias. On satellite images en-echelon structures are visible (Fig. 1). The uplifted Campanian–Turonian limestones of the pressure ridges sampled were deformed at depths of 2–5 km (Janssen et al., 2004). The faulting intensity is rather weak at outcrop scale, but the microstructures reveal a substantial internal deformation.

While to the North of the study area the fault structure can be assessed from surface geological studies (e.g., Niemi et al., 2001), large parts of the study area itself (south of 30°35′ N, Fig. 1) are covered by young sediments (fluviatile and aeolian sands) obscuring the structure of the fault and its surrounding, and limiting the outcrop extent at the fault. Even the scarce outcrops do not exhibit the typical fault zone architecture with fault core (gouge zone), damage zone and undeformed

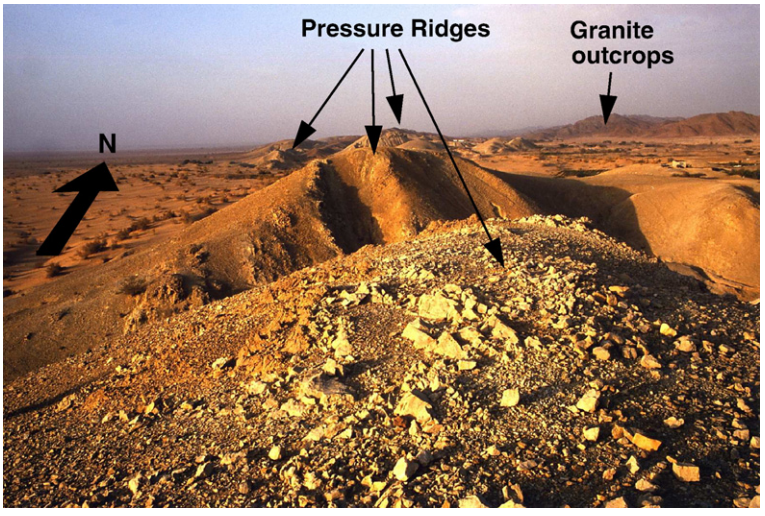

Fig. 2. View of the pressure ridges in the northern part of the study area. View toward the North.

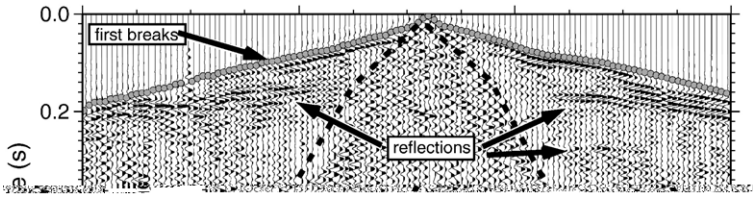

Fig. 3. Typical data example of a shot gather, line 7, shot 37. Data is bandpass filtered. Note the good signal to noise ratio of the first arrivals (indicated by small grey circles), and the strong ground roll generated by our shallow sources which was manually removed (muted; below dashed black lines).

host rock as described for other major fault zones (Chester and Logan, 1986; Chester et al., 1993; Faulkner et al., 2003).

3. Experiment, data & processing

In October 2001 a high-resolution, small-scale seismic experiment (Controlled Source Array, CSA II) was conducted at the WAF between 30°31′ N and 30°36′ N (see Fig. 1). 8 seismic lines, each with a length of 1 km, were deployed across the fault (centered on the surface fault trace). The spacing between the seismic lines was 1 km (except for the three southernmost lines which were 2 km apart), so that information on the shallow-most volume of the target area at about 10 km fault length was obtained.

Each line was equipped with 200 geophones with a spacing of 5 m. We used a SUMMIT datalogger running with a sample rate of 0.0625 ms and 4.5 Hz vertical component seismometers (Type SM-6, SENSOR Nederland). Each line had 50 shots with a spacing of 20 m. The shots (300 g of explosives) were detonated in 1 to 1.5 m deep boreholes. All channels of a particular line recorded all shots on this line. The data were resampled to a sample rate of 1 ms, and the geometry was installed using a differential GPS system with a lateral accuracy of 0.5 m.

Fig. 3 shows a typical example of a shot gather (line 1, shot 25 in the center of the spread). The energy of most of the shots was sufficient to observe the direct P arrival over the maximum observation distance (offset) of 1 km. However, the explosive sources in our shallow boreholes also produced strong surface waves/ground roll.

4. Tomography — method, processing and resolution analysis

Due to the good signal to noise ratio of the direct P-waves, up to 10.000 manually determined first break (P-wave) onset times could be used for each line (Maercklin, 2004). Fig. 4 shows all picks along line 1. S-wave generation was low, so no S-wave models were produced. Data were inverted following a tomographic method outlined in Zelt and Barton (1998), resulting in 8 independent models (Fig. 6). Since in tomographic inversions with sources and receivers at the surface the resolution decreases with depth and in order to increase the stability of the inversion procedure, an iterative approach calculating inversion runs with decreasing block size was used. In the successive inversions the

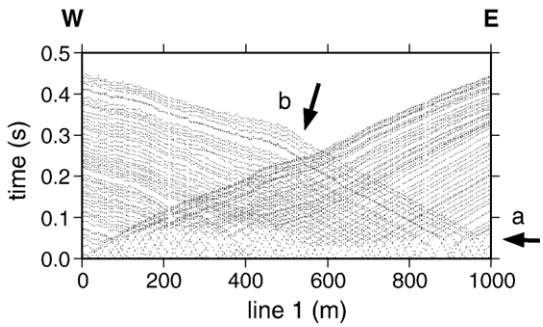

Fig. 4. All travel time picks of the P wave (first) arrivals for line 1. Each of the 9800 dots represents one first break reading along this line. Clearly visible are the bend in the travel-time curves between 0.04 and 0.08 s which corresponds to a velocity gradient between 20 and 40 m depth (a), and a prominent bend in the travel time curve for longer offsets at $x = 500$ m which corresponds to a large horizontal velocity gradient at the WAF (b, compare also to Fig. 6).

respective starting model was given by the final velocity model of the previous run. In the last (final) inversion run we used a grid spacing of 10 × 10 m in the least squares inversion. This approach makes the inversion very robust with respect to the choice of the starting model. For the finite difference calculation of the travel times (ray tracing) a grid spacing of 5 × 5 m was used (Vidale, 1988). Our approach yields relatively smooth models at greater depth and high resolution at the surface.

As expected from the experiment geometry, the hit count (number of rays crossing the individual inversion block) was generally very high close to the surface (>1.000) and decreased quickly with depth. Interpreting the hitcount as a proxy for the resolution, we generally have a high spatial resolution at the surface which decreases significantly with depth. In order to further check the resolution of our analysis we conducted tests with synthetic models (checker board recovery models). Following common practice, we calculated synthetic traveltimes (for the actual source and receiver geometry) through regular synthetic models, added random noise, and inverted the travel time data in the same way as the real data. The synthetic models consisted of spatially alternating perturbations (±5%) of a reasonable, realistic background velocity distribution. Inspection of the recovery of the regular synthetic model allows the estimation of the resolution in different parts of the model for a given size of anomalies. Fig. 5 shows the results of these checker board tests for three different block sizes. The same inversion parameters, i.e. iteratively decreasing block size, smoothing, etc. as for the inversion of the observed data were used. The checkerboard results suggest that in the central parts of the profiles structures with a lateral extent in the order of 100 m are well resolved down to a depth of 150 m. Smaller inhomogeneities (50 or 25 m size) are only resolved down to 100 m or 70 m depth, respectively.

The final RMS misfit between the observed and predicted travel times is of the order of 0.005 s. Tests with randomly chosen subsets of the complete data sets gave velocity models which are very similar to the final models. The main velocity anomalies found for the inversion of the complete data set do not change their position and magnitude in the inversion with subsets of the data. This is a further indication that the features of the velocity models are robust.

5. Reflection seismics — method and processing

For the CDP processing the data were band-pass filtered (10–80 Hz), field statics corrections (replacement velocity 1000 m/s; datum at sea level) applied, and noisy traces removed. Sections contaminated by strong ground roll were muted (see Fig. 3), a procedure often applied to shallow seismic data (e.g., Baker, 1999; Hawman et al., 2000). In the center of each line the maximum nominal fold of 25 is reached.

The stacking of refracted arrivals and, in turn, the misinterpretation of these signals as reflections is a common pitfall in shallow seismic data analysis (e.g., Büker et al., 1998; Baker, 1999). Application of a conservative NMO stretch mute to our data reduced unwanted stacking of first arrivals to a large extend. However, in order not to remove or degrade very shallow reflections (i.e. at times <100 ms) we chose not to apply further (surgical) first break mutes (see also Shtivelman et al., 1998). Accordingly, the top-most parts of our stacked sections may contain a certain amount of refracted energy (first arrivals). Furthermore, on some sections energy presumably related to very-near-surface structures beneath the sources and/or receivers and arriving after the first breaks (site effects) might also be contained in the stacked data (see also Maercklin et al., 2005).

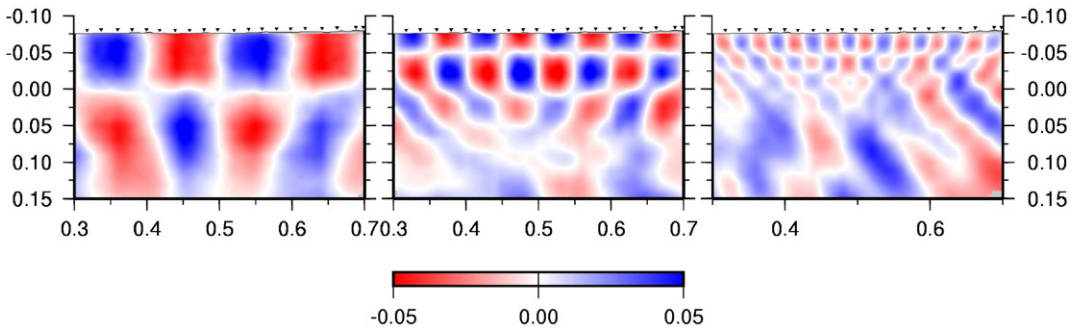

Fig. 5. Results of the checkerboard resolution tests with different size of anomalies (100, 50 and 25 m). Structures with a size of 100 m are well resolved down to a depth of 150 m, smaller inhomogeneities (50 or 25 m size) are resolved down to 100 m or 70 m depth, respectively. Color scale corresponds to ±5% velocity perturbation of the background model; horizontal and depth scales in km. See text for more information.

Stacking velocities were determined from conventional velocity analysis (e.g., Yilmaz, 1987) using series of constant velocity stacks (Maercklin, 2004). The CDP stacks for all lines are given in Fig. 7. In an attempt to move the reflections to their correct spatial position (and to allow direct comparison with the tomographic images) we migrated the stacked sections with a 2-D phase-shift (depth) migration (Gazdag, 1978; Gazdag and Sguazzero, 1984). For the migration the smoothed velocity models from the first-break tomography for the shallow parts were used, for the deeper parts we resort to the velocity model by Maercklin et al. (2005). Fig. 8 gives the migrated sections. Small variations of the velocity models and even the application of 1-D time migration (Gazdag, 1978) and corresponding depth conversion yielded similar results.

6. Results

Fig. 9 is a composite figure showing both migrated seismic sections overlain on the velocity models, together with the interpretation.

The velocity models of lines 1 to 7 (Fig. 6) show lower velocities in the eastern part (predominantly blue colors, $v_p \leq 2$ km/s down to 200 m) and higher velocities in the western half (already v_p~3 km/s at a depth range of about 50 m). A strong lateral gradient was also visible at greater depths (deeper than 1 km) in previous studies, however, at these larger depth the distribution of faster and slower areas was reversed, i.e. with higher velocities in the East and lower velocities in the West (Ritter et al., 2003; Maercklin et al., 2005; Tasarova et al., 2006). The change of the velocities from the East to the West in the shallow part (top 200 m) generally correlates well with the surface trace of the WAF (in all profiles at about 500 m except in line 3 where the fault trace is found approximately at 400 m). In the three northern profiles (8, 9, 10) high velocities (larger than 4.5 km/s) are found at a depth of 30 to down to 200 m at the eastern side of the WAF. These correlate with the granites cropping out just North of profile 10 (see Fig. 1). Purple colors in the top most meters (around 1.0 km/s) are due to sand dunes (lines 1, 3, 5, 8, 9). In the high-resolution tomographic pictures we see no indication for a faultzone related low-velocity zone as found at other large fault zones (see below for discussion).

At first glance the overall reflectivity is relatively weak, and the reflection seismic images show a large variety. Most of the sub-parallel profiles are only 1 km apart, but their reflective character can change significantly. However, at a closer look certain features can be identified, correlated, and traced between the sections.

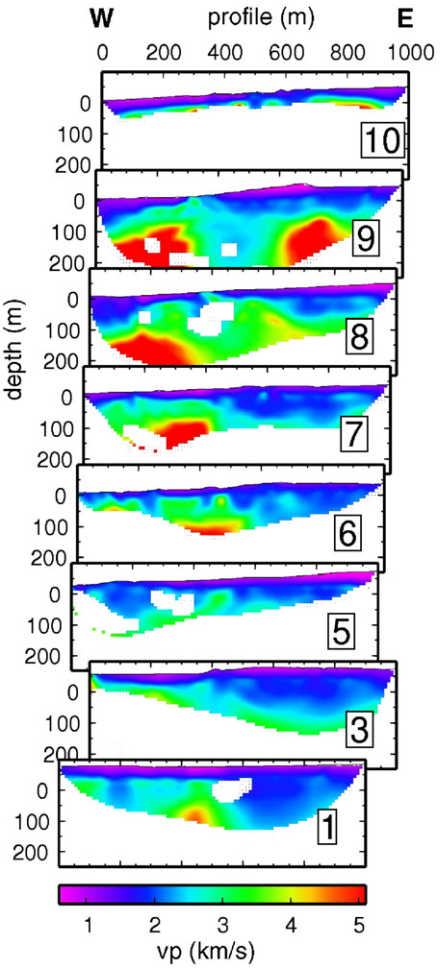

Fig. 6. Results of the tomographic inversion. Seismic P wave velocities are color coded (see scale at the bottom), unresolved regions are masked (white).

The strongest reflections appear in the top 300 m, and they belong most likely to superficial sedimentary layers (labeled "C" in the summarizing Fig. 9). On almost all profiles they are weaker at the center of the profiles. This might be due to stronger deformation in the center, i.e. at the location of the main fault. Different velocities in the Eastern and Western parts of the sections (see above) indicate different composition and material of the sediments at shallow depth. Toward the central portions of almost all profiles (centered on the surface trace of the WAF, lines 1, 3, 5, 7, 8, 9, 10) these reflections are bent upward. The shallowest reflections appearing on lines 3, 5, and 7 are mostlikely due to a superposition of near-surface reflected and refracted signals and are therefor not considered in the interpretation.

Also on almost all profiles we notice a pronounced difference in the reflection pattern in the Eastern and

Western parts of the sections (Fig. 8), often changing quite abruptly at the WAF. In some profiles the subhorizontally aligned reflectors are disrupted here. This is mainly found on lines 1, 6, and 7, but also on lines 3 and 5. We interpret this as the main strand of the WAF (labeled "M" in Fig. 9) separating two different

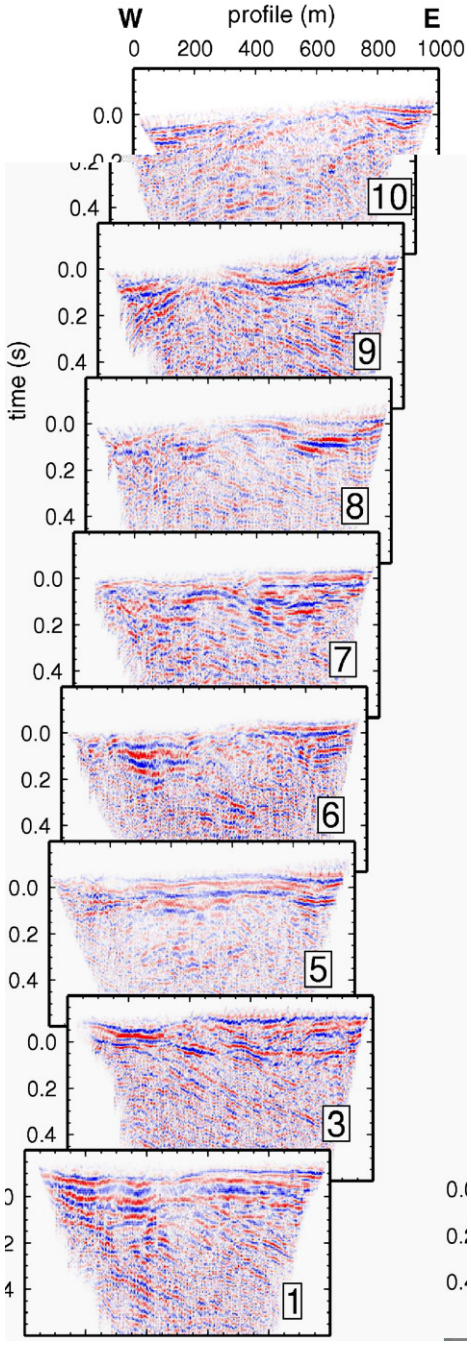

Fig. 7. Final reflection seismic stacks of all 8 lines. Positive and negative amplitudes are shown in blue and red wiggles.

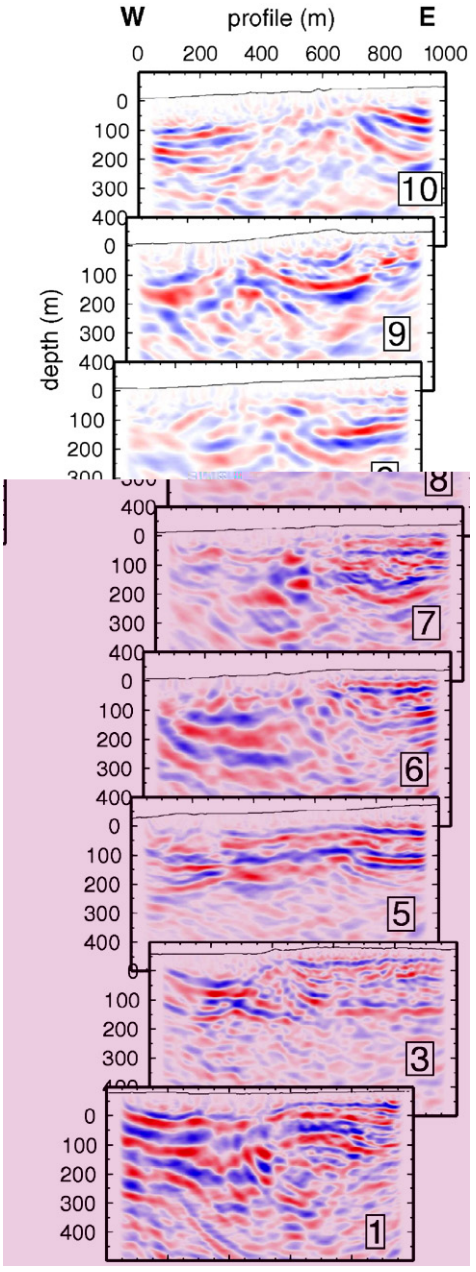

Fig. 8. Migrated reflection seismic sections of all lines. Positive and negative amplitudes are shown in blue and red wiggles.

blocks (formed by different younger strata/sediments at shallow depths). There are no indications for a dip of the fault zone in the top 500 m. The central portion of profile 10 is formed by a 400 m wide zone of diffuse reflectivity, and prominent and upward-bent reflectors are found at the ends of the profile. Unfortunately, due to higher velocities in the northern part of the study area and failures during the acquisition of line 10, the

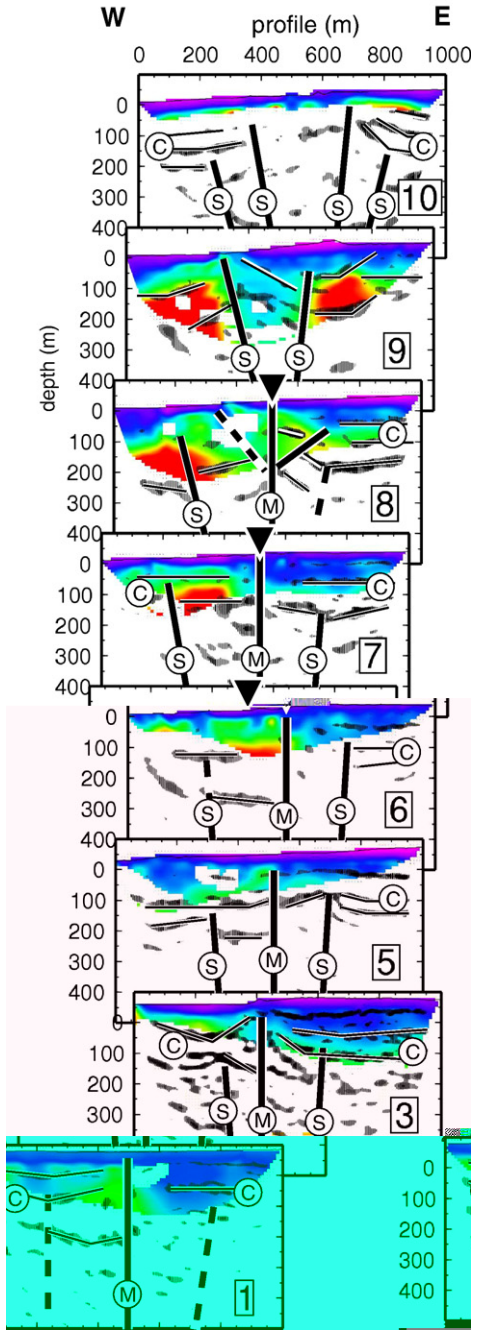

Fig. 9. Migrated reflection seismic images (black wiggles) overlaid on the tomography (color coded) together with our geological interpretation (for scale of seismic p-velocities see Fig. 6). Black thick lines indicate inferred faults, dashed lines indicate less well constrained faults. M), S), and C) indicate the main fault, secondary/flanking faults, and sedimentary cover at the two sides, respectively. Inverted triangles indicate the position of guided wave observations from (Haberland et al., 2003). For more information see text.

velocity model on this line is restricted to less than 50 m depth.

In the unmigrated stacks (Fig. 7) eastward dipping events are visible on many sections. They most likely represent reflections at steeply dipping or near vertical structures in the center of the profiles (i.e. the main fault) and/or parts of diffraction hyperbolas related to strong point scatterers directly at the fault (see for example Hole et al., 2001). In the migration process (Fig. 8) these reflective events collapse into subvertical structures or single points. They give further evidence that there is an abrupt change of material (with different properties) at the position of the fault.

On several profiles indications for secondary faults (indicated by "S" in Fig. 9) are visible West (lines 5, 6, 7, 8, 9, 10) and East (lines 3, 5, 6, 8, 10) of the main strand, respectively. As in the case of the "main" fault strand they are also indirectly deduced from separated and/or disrupted subhorizontally aligned reflective elements. At line 5 and 8 they are best expressed. These fault branches seem to dip toward the center indicating a flower structure. Covering strata at different depths are bent upward toward the center indicating an upward (syn-sedimentary) movement of the slivers in between the flanking faults. At lines 5 and 8 these positive flower structures seen in the reflection seismic images correlate very well with the tomographic velocities showing elevated velocities in the pressed-out/up-lifted slivers. At profile 5 this positive flower structure seems to be buried by 100 m thick sediments.

Profiles 3 and 9 exhibit the most complex structures. Line 3 shows reflective elements West of the presumed surface trace (in this profile at about 400 m) which dip toward the East. Since it is conceivable that the strong reflectors originate from impedance contrasts within the sedimentary layering we suggest that the latter reflectors image the internal structure of the sliver of pushed-up material which is characterized by easterly dipping beds. In line 9 we also observe characteristic dipping reflectors approaching the surface at $x=370$ m which might reflect the internal structure of the pushed-up slivers. However, the still relatively large distance between neighboring lines (with respect to the obviously highly variable geological structures) does not allow a univocal interpretation of these structures in 3D (lines 3 and 9). Furthermore we also have to consider off-line effects (out-of-plane reflections from positions North and South of the respective lines; not unlikely in this complex geological setting).

7. Discussion

The images show a complex structure of the WAF at shallow depth in the study area and characterize it as a

rather broad, 100 to 300 m wide heterogeneous zone of deformed and displaced material. A summarizing sketch is shown in Fig. 10. A through-going main fault can thus be assumed. In the North and at several positions along the fault clear evidence for positive flower structures is found. The surface expressions of these flower structures are the pressure ridges with outcroppings of cretaceous limestones in the northern part of the study area (Garfunkel et al., 1981; Atallah, 1992; Ginat et al., 1998). In the southern part of the study area the structures are buried by up to 100 m thick young sediments/sand dunes.

The positive flower structures are typical indications for a transpressional regime (Harding and Lowell, 1979; Lowell, 1985). Splinter of material or layers pushed-up by this material forms the pressure ridges/push-ups at

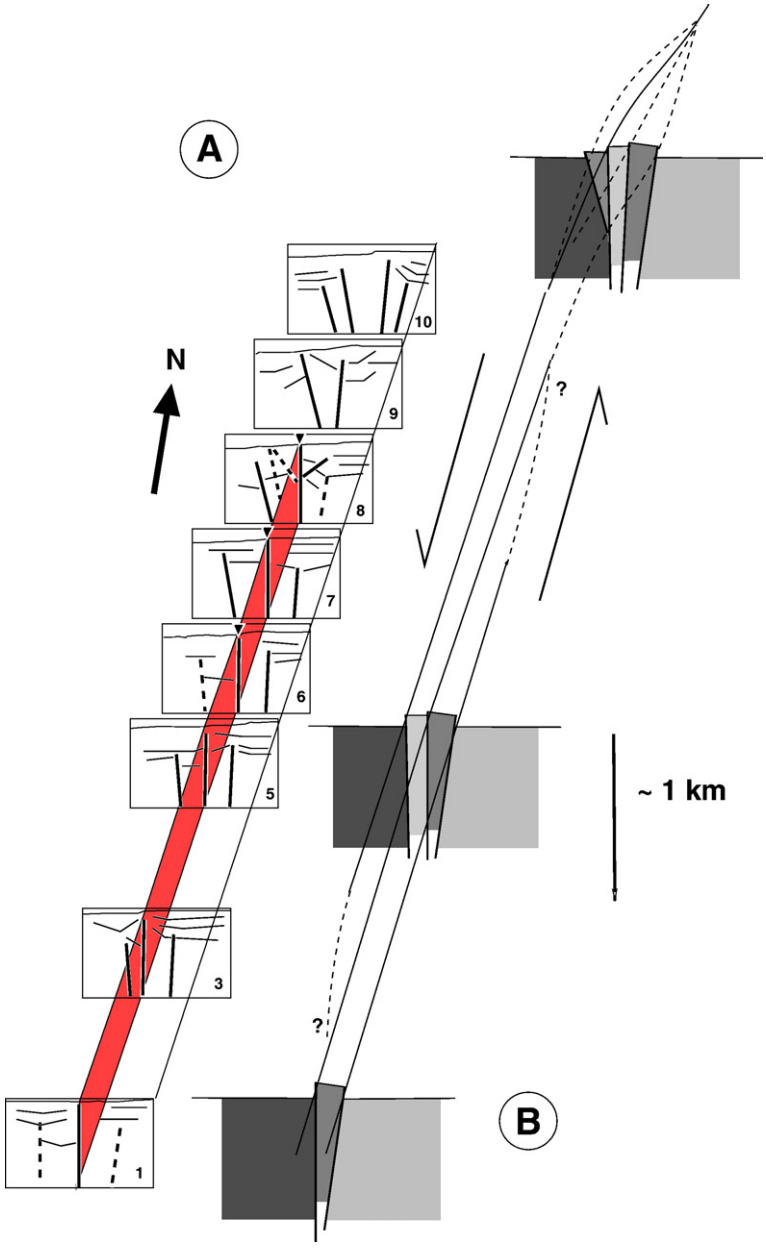

Fig. 10. A) Summary of all interpreted sections along the fault (perspective view from the South). The main fault is indicated by the red area. B) Possible reconstruction of the fault structure based on the seismic results. A few subparallel faults form the WAF system in the study area; to the North the pressure ridge structure dominates. Covering sediments are omitted. See text for further explanation.

the surface. However, along-strike these pushed-up wedges can form complex and broader structures resembling horizontal duplexes (Sheriff, 1991; Twiss and Moores, 1992; Hancock, 1994). Here, the pressure ridges and the positive flower structures in the northern part of the study area can be related to the slight change of fault orientation north of 30°36′ N, Fig. 1.

However, we have indications for subparallel faults at almost all profiles (with increasing degree of complexity from South to North). At the mesoscopic scale the sub-parallel faults are only a few hundred meters apart (at the surface). In industry reflection profiles in the region, indications for further sub-parallel faults at larger offset from the main fault trace and larger scale flower structures had been found. They are observed at the southern part of the WAF (Shtivelman et al., 1998; Zilberman et al., 2005), at the eastern branches of the DST in Israel (Frieslander, 2000) and also in the study area (Kesten, 2004; Kesten et al., in press). However, the structures in the western north-central Araba valley (i.e., the WAF and the faults in its direct vicinity) do not show the normal component as the faults in the eastern Araba valley (Frieslander, 2000).

It seems that the main fault is a through-going, though narrow feature in the study area. Between lines 6 and 8 we have a clear indication for the continuity of the main fault strand near the surface (with a narrow waveguide of between 3 and 12 m width) from the observation of guided waves (see inverted triangles in Fig. 9, Haberland et al. (2003)). However, the profiles presented here are 1 to up to 2 km apart, so it cannot unambiguously be stated how the other (secondary) faults identified in the individual profiles, are connected. They might form sub-parallel fault segments stretching over many kilometers (merging at greater depth with the main fault) or constitute a network of (anastomosing) faults at different scales. Since at the surface sub-parallel lineaments of some kilometers length (scarps, elongated limestone outcrops, etc.) can be seen, and considering on the other hand that some structures are only seen in single profiles, we assume that the WAF shows both characteristics in its shallow part. In trenching analysis, Niemi et al. (2001) found also sub-parallel fault strands, pressure ridges and comparable narrow fault zones at the WAF zone approximately 50 km N of our study area. At a segment about 200 km further to the north, the main faults of the DST are observed as wide zones of deformation rather than as distinct fault planes (Rotstein et al., 1992).

The imaging methods used here do not show evidence for a single wide damage zone as being the classical, characteristic element of a typical large brittle fault zone structure (Chester and Logan, 1986; Scholz, 1987). A broader low-velocity region occurs only on line 8 (between 300 and 600 m, Figs. 6 and 9) and is therefore only a local feature. We observed a network of (subparallel or anastomosing) individual faults which seem to be characterized by rather narrow fault cores/damage zones. These narrow fault zone widths (between 3 and 12 m) were revealed by a guided wave study (Haberland et al., 2003). We would not expect such narrow features to be imaged by our tomographic models due to the given, although dense, station geometry (see also checkerboard test, Fig. 5). These faults form a broad heterogeneous zone of deformed and displaced material, which, however, is not characterized by low seismic velocities at a larger scale. Through-going, sub-vertical low-velocity layers with a typical width of 100 to 300 m had been found at many other large shear zones such as the SAF, the Carlsberg fault zone, the North Anatolian fault and many more (e.g. Li et al., 1997, 1998; Ben-Zion et al., 2003; Nielsen et al., 2005; Lewis et al., 2005). They had been interpreted as the fault damage zone where the crushed and damaged material causes a net-reduction of the seismic velocities. Often these zones also show enhanced electrical conductivities (due e.g. to circulating fluids). This characteristic is also not found at the WAF down to a depth of 4 km (Ritter et al., 2003, 2004).

It is instructive to relate the thickness of the low velocity zone to the slip on the fault and compare with the thickness of gouge in experiments of wear mechanics. The ratio of gouge thickness to total slip is of order 0.0001–0.001, depending on normal stress (Scholz, 2002, Fig. 2.14, p.79). For a depth of 0.5 km we may take a normal stress of 10 MPa giving 0.0002 (granite) to 0.0005 (sandstone). Allowing for a range of thickness of the fault-related low-velocity zone of 5–20 m (in agreement with the findings of the guided wave study), the corresponding total slip would vary between 10 and 100 km.

This is the range of uncertainty of the total offset across the WAF. Eyal et al. (1986) reconstruct 25 km of shear distributed on inactive fault strands in the Sinai block, west of the active Gulf of Aqaba. The western shoulder of WAF does not expose basement, and studies of slip distribution are not available, but at least two strands strike parallel to WAF within the rift, and are likely to absorb some of the geological deformation (see also Frieslander, 2000).

We speculate that the apparent distribution of deformation across several fault strands and the concentration of the deformation to individual narrow fault zones might be related to the low loading to healing

ratio. Today the seismicity at the DST/WAF segment is moderate, and the recent slip rate is quite low. At the WAF the seismicity is clustered (in time) and large earthquakes occur in a long cycle (Marco et al., 1996; Amit et al., 2002; Marco and Agnon, 2005). Lyakhovsky et al. (2001) have analyzed the behavior of fault networks aided by a damage rheology model. They find that where the rate of healing is large compared to the rate of loading the system exhibits short memory and fault geometry evolves along several seismic cycles. The low rate of loading on the WAF is compatible with such a system, and with the distribution of the total slip across several strands, each active at a different time.

Geochemical data suggest reduced fluid rock interactions and limited fluid flow related to the WAF (Janssen et al., 2004, 2005). Because of the absence of a wide through-going fault core the fault probably does not act as an important fluid conduit. Such a scenario is remarkably different from the northern branches of the DST (Gomez et al., 2001; Meghraoui et al., 2001) and also from many other large and active fault zones (e.g. West Fault Zone in Chile, Hoffmann-Rothe et al., 2004, San Andreas Fault in California, Chester et al., 1993; Unsworth et al., 2000).

8. Conclusions

We used tomographic and reflection seismics imaging together with geological and geochemical analysis to reveal the shallow architecture of the WAF as part of the DST. The application of these complementary methods allowed the identification of a complex structure exhibiting a broad heterogeneous zone forming the fault zone at shallow depth. The main findings of this study are:

- Clear evidence for a subvertical (main) fault in the top-most 500 m separating two blocks with different seismic (physical) properties.
- Indication for subparallel faults flanking the main fault, thus forming a typical flower structure. Towards the south these structures are covered by Holocene sediments/sand dunes.
- Shallow reflectors related to superficial sediments are often bent upward toward the center of the profiles indicating an upward movement of the splinters thus forming positive flower structures. In the North these structures correspond to the transpressional elements at the surface (pressure ridge) caused by the restraining eastward bend of the fault course.
- The fault cores/damage zones of the individual fault(s) seem to be very narrow. On a larger scale a network of sub-parallel faults and flower structures is formed.

The WAF in the North-central Wadi Araba Valley therefore shows elements of a mature strike–slip fault zone with a strong localization of deformation at depth and the distribution of deformation over complex (transpressional) structures close to the surface. This broad heterogeneous zone of deformed and displaced material is, however, not characterized by low seismic velocities. This puts this fault in contrast to other large active faults where a wider fault-related low-velocity channel had been observed. We suggest that this structure is a direct consequence of the particular low loading to healing ratio at this DST segment compared to other large shear zones.

Acknowledgements

The CSA II project (as part of the DESERT project) was financed by the GeoForschungsZentum Potsdam (GFZ). Instruments were provided by the GIPP (GFZ Potsdam). We thank our contractor Chemical and Mining (Jordan) for explosives, and the National Resources Authorities of Jordan (NRA) for logistical support. Thanks to Y. Bartov for stimulating discussions. Furthermore we thank the residents of Bir Mathkur for their cooperation, and all field groups for their excellent work under difficult conditions. The manuscript benefited greatly from critical remarks and suggestions by editor Kevin Furlong, reviewer John Hole, and an anonymous reviewer.

References

Abu Taimeh, I.A.E., 1988. Structural and applied remote sensing studies at Gharandal-Petra area, eastern Wadi Araba. Master's thesis, University of Jordan, Jordan.

Amit, R., Zilberman, E., Enzel, Y., et al., 2002. Paleoseismic evidence for time dependency of seismic response on a fault system in the southern Arava Valley, Dead Sea rift, Israel. Geol. Soc. Amer. Bull. 114 (2), 192–206.

Atallah, M., 1992. Tectonic evolution of the northern Wadi Arava, Jordan. Tectonophysics 204, 17–26.

Baker, G.S., 1999. Processing Near-Surface Seismic-Reflection Data: A Primer. No. volume in Course Notes Series. Society of Exploration Geophysicists, Tulsa, Oklahoma.

Barjous, M., Mikbel, S., 1990. Tectonic evolution of the Gulf of Aqaba — Dead Sea Transform fault system. Tectonophysics 180, 49–59.

Barjus, M., 1988. Structural study of the area between Petra and Ash Shaw-back. Master's thesis, University of Jordan, Jordan.

Bartov, Y., Avni, Y., Calvo, R., Frieslander, U., 1998. The Zofar Fault — A major intra-rift feature in the Arava rift valley. GSI Curr. Res. 11, 27–32.

Ben-Avraham, Z., 1985. Structural framework of the Gulf of Elat (Aqaba), northern Red Sea. J. Geophys. Res. 90, 703–726.

Ben-Zion, Y., Sammis, G., 2003. Characterization of fault zones. Pure Appl. Geophys. 160, 677–715.

Ben-Zion, Y., Peng, Z., Okaya, D., Seeber, L., Armbruster, J.G., Ozer, N., Michael, A.J., Baris, S., Aktar, M., 2003. A shallow fault zone structure illuminated by trapped waves in the Karadere–Duzce branch of the North Anatolian Fault, western Turkey. Geophys. J. Int. 152, 1–19.

Bowman, D., King, G., Tapponnier, P., 2003. Slip partitioning by elastoplastic propagation of oblique slip at depth. Science 1121–1123.

Büker, F., Green, A.G., Horstmeyer, H., 1998. Shallow seismic reflection study of a glaciated valley. Geophysics 63 (4), 1395–1407.

Chester, F., Logan, X., 1986. Implications for mechanical properties of brittle faults from observations of the Punchbowl fault zone, California. Pure Appl. Geophys. 124 (1/2), 79–106.

Chester, F.M., Evans, J.P., Biegel, R.L., 1993. Internal structure and weakening mechanisms of the San Andreas Fault. J. Geophys. Res. 98 (B1), 771–786.

DESERT Team, 2004. The crustal structure of the Dead Sea Transform. Geophys. J. Int. 156. doi:10.1111/j.1365-246X.2004.02143.x.

Eyal, Y., Eyal, M., Bartov, Y., Steinitz, G., Folkman, Y., 1986. The origin of the Bir Zreir rhomb-shaped graben, eastern Sinai. Tectonics 5 (2), 267–277.

Faulkner, D., Lewis, A., Rutter, E., 2003. On the internal structure and mechanics of large strike–slip faults: field observations from the Carboneras fault, southeastern Spain. Tectonophysics 367, 235–251.

Frieslander, U., 2000. The structure of the Dead Sea Transform emphasizing the Arava, using new geophysical data. Ph.D. thesis, Hebrew University, Jerusalem, in Hebrew.

Gardosh, M., Kashai, E., Salhov, S., Shulman, H., Tannenbaum, E., 1997. Hydrocarbon exploration in the southern Dead Sea Basin. In: Niemi, T.M., Avraham, Z.B., Gat, J.R. (Eds.), The Dead Sea, The lake and its setting. Oxford monographs on Geology and Geophysics, pp. 57–72.

Garfunkel, Z., 1981. Internal structure of the Dead Sea leaky transform (rift) in relation to plate kinematics. Tectonophysics 80, 81–108.

Garfunkel, Z., 1997. The history and formation of the Dead Sea basin. In: Niemi, T.M., Avraham, Z.B., Gat, J.R. (Eds.), The Dead Sea, The lake and its setting. Oxford monographs on Geology and Geophysics, pp. 36–56.

Garfunkel, Z., Zak, I., Freund, R., 1981. Active faulting in the Dead Sea Rift. Tectonophysics 80, 1–26.

Gazdag, J., 1978. Wave equation migration with phase-shift method. Geophysics 43 (7), 1342–1351.

Gazdag, J., Sguazzero, P., 1984. Migration of seismic data by phase shift plus interpolation. Geophysics 49 (2), 124–131.

Ginat, H., Enzel, Y., Avni, Y., 1998. Translocated plio-pleistocene drainage systems along the Arava fault of the Dead Sea Transform. Tectonophysics 284 (1–2), 151–160.

Ginzburg, A., Kashai, E., 1981. Seismic measurements in the southern Dead Sea. Tectonophysics 80, 67–80.

Gomez, F., Meghraoui, M., Darkal, A., Hijazi, F., Suleiman, Y., Sbeinati, R., Darawcheh, R., Al-Ghazzi, R., Barazangi, M., 2001. Holocene paleoseismic activity of the Serghaya branch of the Dead Sea fault system in Syria and Lebanon. EOS Trans. AGU 82 (47) (S52C-0649).

Haberland, C., Agnon, A., El-Kelani, R., Maercklin, N., Qabbani, I., Ruempker, G., Ryberg, T., Scherbaum, F., Weber, M., 2003. Modelling of seismic guided waves at the Dead Sea Transform. J. Geophys. Res. 108 (B7). doi:10.1029/2002JB002309.

Hancock, P.L. (Ed.), 1994. Continental Deformation. Pergamon Press.

Harding, T.P., Lowell, J., 1979. Structural styles, their plate-tectonic habitats, and hydrocarbon traps in petroleum provinces. Am. Assoc. Petrol. Geol. Bull. 63 (7), 1016–1058.

Hawman, R.B., Prosser, C.L., Clippard, J.E., 2000. Shallow seismic reflection profiling over the Brevard zone, South Carolina. Geophysics 65 (5), 1388–1401.

Hoffmann-Rothe, A., Ritter, O., Janssen, C., 2004. Correlation of electrical conductivity and structural damage at a major strike–slip fault in northern Chile. J. Geophys. Res. 109 (B10), B10101.

Hole, J.A., Catchings, R.D., St. Clair, K.C., Rymer, M.J., Okaya, D.A., Carney, B.J., 2001. Steep-dip seismic imaging of the San Andreas fault near Parkfield. Science 294, 1513–1515.

Janssen, C., Romer, R.L., Hoffmann-Rothe, A., Kesten, D., Al-Zubi, H., 2004. The Dead Sea Transform: evidence for a strong fault? J. Geol. 112, 561–575.

Janssen, C., Romer, R.L., Hoffmann-Rothe, A., Mingram, B., Dulski, P., Mller, P., Al-Zubi, H., Group, D.R., 2005. The role of fluids in faulting deformation: a case study from the Dead Sea Transform (Jordan). Int. J. Earth Sci. 94 (2), 243–255.

Joffe, S., Garfunkel, Z., 1987. The plate kinematics of the circum Red Sea — a reevaluation. Tectonophysics 141, 5–22.

Kashai, E.L., Croker, P.F., 1987. Structural geometry and evolution of the Dead Sea — Jordan rift system as deduced from new subsurface data. Tectonophysics 141, 33–60.

Kesten, D., 2004. Structural observations at the Southern Dead Sea Transform from Seismic Reflection Data and ASTER Satellite Images. Ph.D. thesis, University of Potsdam, Germany.

Kesten, D., Weber, M.H., Haberland, C., Janssen, C., Agnon, A., Bartov, Y., DESERT Group, in press. Combining satellite and seismic images to analyze the shallow structure of the Dead Sea Transform near the DESERT transect. Int. J. Earth Sci.

Klinger, Y., Avouac, J., Dorbath, L., Karaki, N.A., Tisnerat, N., 2000. Seismic behaviour of the Dead Sea fault along Araba valley, Jordan. Geophys. J. Int. 142, 769–782.

Lewis, M., Peng, Z., Ben-Zion, Y., Vernon, F., 2005. Shallow seismic trapping structure in the San Jacinto fault zone near Anza, California. Geophys. J. Int. 162, 867–881.

Li, Y.-G., Aki, K., Adams, D., Hasemi, A., Lee, W.H., 1994. Seismic guided waves trapped in the fault zone of the Landers, California, earthquake of 1992. J. Geophys. Res. 99 (B6), 11,705–11,722.

Li, Y.-G., Ellsworth, W.L., Thurber, C.H., Malin, P.E., Aki, K., 1997. Fault-zone guided waves from explosions in the San Andreas fault at Parkfield and Cienega Valley, California. Bull. Seismol. Soc. Am. 87 (1), 210–221.

Li, Y.-G., Aki, K., Vidale, J.E., Alvarez, M.G., 1998. A delineation of the Nojima fault ruptured in the M 7.2 Kobe, Japan, earthquake of 1995 using fault zone trapped waves. J. Geophys. Res. 103 (B4), 7247–7263.

Lowell, J.D., 1985. Structural Styles in Petroleum Exploration. OGCI Publications.

Lyakhovsky, V., Ben-Zion, Y., Agnon, A., 2001. Earthquake cycle, fault zones, and seismicity patterns in a rheologically layered lithosphere. J. Geophys. Res. 106 (B3), 4103–4120.

Maercklin, N., 2004. Seismic structure of the Arava fault, Dead Sea Transform. Ph.D. thesis, Universität Potsdam.

Maercklin, N., Haberland, C., Ryberg, T., Weber, M., Bartov, Y., DESERT Group, 2004. Imaging the Dead Sea Transform with scattered seismic waves. Geophys. J. Int. 158 (1), 179–186.

Maercklin, N., Bedrosian, P.A., Haberland, C., Ritter, O., Ryberg, T., Weber, M.H., Weckmann, U., 2005. Characterizing a large shear-zone with seismic and magnetotelluric methods — the case of the Dead Sea Transform. Geophys. Res. Lett. doi:10.1029/2005GL022724.

Marco, S., Agnon, A., 2005. High-resolution stratigraphy reveals repeated earthquake faulting in Masada Fault Zone, Dead Sea Transform. Tectonophysics 408, 101–111.

Marco, S., Stein, M., Agnon, A., Ron, H., 1996. Long-term earthquake clustering: A 50,000-year paleoseismic record in the Dead Sea Graben. J. Geophys. Res. 101 (B3), 6179–6191.

Mechie, J., Abu-Ayyash, K., Ben-Avraham, Z., El-Kelani, R., Mohsen, A., Rümpker, G., Saul, J., Weber, M., 2005. Crustal shear velocity structure across the Dead Sea Transform from two-dimensional modelling of desert project explosion seismic data. Geophys. J. Int. 160 (3), 910–924.

Meghraoui, M., Gomez, F., Sbeinati, R., Van der Woerd, J., Mouty, M., Hijazi, F., Darkal, A., Darawcheh, R., Radwan, V., Al-Najjar, H., Layous, I., Al-Ghazzi, R., Barazangi, M., 2001. Late holocene paleoseismic timing and slip history along the Missyaf segment of the Dead Sea Fault in Syria. EOS Trans. AGU 82 (47) (S52C-0648).

Mohsen, A., Hofstetter, R., Bock, G., Kind, R., Weber, M., Wylegalla, K., Rümpker, G., Group, D., 2005. A receiver function study across the Dead Sea Transform. Geophys. J. Int. 160 (3), 948–960.

Neev, D., Hall, J.K., 1997. Geophysical investigations in the Dead sea. Sediment. Geol. 23.

Nielsen, L., Thybo, H., Jørgensen, M.I., 2005. Integrated seismic interpretation of the Carlsberg Fault zone, Copenhagen, Denmark. Geophys. J. Int. 2 (2), 461–478.

Niemi, T.M., Zhang, H., Atallah, M., Harrison, J.B.J., 2001. Late pleistocene and holocene slip rate of the Northern Wadi Araba fault, Dead Sea Transform, Jordan. J. Seismol. 5, 449–474.

Ritter, O., Ryberg, T., Weckmann, U., Hoffmann-Rothe, A., Abueladas, A., Garfunkel, Z., DESERT Group, 2003. Geophysical images of the Dead Sea Transform in Jordan reveal an impermeable barrier for fluid flow. Geophys. Res. Lett. 30 (14). doi:10.1029/2003GL017541.

Ritter, O., Hoffmann-Rothe, A., Bedrosian, P.A., Weckmann, U., Haak, V., 2004. Electrical conductivity images of active and fosil fault zones. High Strain Zones: Structure and Physical Properties, vol. 245. The Geological Society, London, pp. 165–186.

Rotstein, Y., Bartov, Y., Hofstetter, A., 1991. Active compressional tectonics in the Jericho area, Dead Sea Rift. Tectonophysics 198, 239–259.

Rotstein, Y., Bartov, Y., Frieslander, U., 1992. Evidence for local shifting of the main fault and changes in the structural setting, Kinarot basin, Dead-Sea Transform. Geology 20 (3), 251–254.

Rümpker, G., Ryberg, T., Bock, G., DESERT Seismology Group, 2003. Boundary-layer mantle flow under the Dead Sea Transform fault inferred from seismic anisotropy. Nature 425, 497–501.

Scholz, C.H., 1987. Wear and gauge formation in brittle faulting. Geology 15, 493–495.

Scholz, C.H., 2002. The Mechanics of Earthquakes and Faulting, 2nd Edition. Cambridge University Press, Cambridge, UK.

Schulz, S.E., Evans, J.P., 2000. Mesoscopic structure of the Punchbowl Fault, Southern California and the geologic and geophysical structure of active strike–slip faults. J. Struct. Geol. 22, 913–930.

Sheriff, R.E., 1991. Encyclopedic Dictionary of Exploration Geophysics. Soc. Explor. Geophys.

Shtivelman, V., Frieslander, U., Zilberman, E., Amit, R., 1998. Mapping shallow faults at the Evrona playa site using high-resolution reflection method. Geophysics 63 (4), 1257–1264.

Stirling, M.W., Wesnousky, S.G., Shimazaki, K., 1996. Fault trace complexity, cumulative slip, and the shape of the magnitude-frequency distribution for strike–slip faults: a global survey. Geophys. J. Int. 124 (3), 833–868.

Tasarova, Z., Goetze, H.-J., El-Kelani, R., Ebbing, J., Hassouneh, M., DESERT Group, 2006. Small-scale gravity modelling of the upper crustal structures in the Araba valley along the Dead Sea Transform. Geochem. Geophys. Geosyst. 7 (Q09012), 1–21.

ten Brink, U.S., Ben-Avraham, Z., 1989. The anatomy of a pull-apart basin: seismic reflection observations of the Dead Sea basin. Tectonics 8, 333–350.

ten Brink, U.S., Rybakov, M., Al-Zoubi, A.S., Hassouneh, M., Frieslander, U., Batayneh, A.T., Goldschmidt, V., Daoud, M.N., Rotstein, Y., Hall, J.K., 1999. Anatomy of the Dead Sea Transform: does it reflect continuous changes in plate motion? Geology 27, 887–890.

Twiss, R.J., Moores, E.M., 1992. Structural Geology. Freeman and Co.

Unsworth, M., Bedrosian, P., Eisel, M., Egbert, G., Siripunarvaporn, W., 2000. Along-strike variations in the electrical structure of the San Andreas fault at Parkfield, California. Geophys. Res. Lett. 27, 3021–3024.

Vidale, J.E., 1988. Finite-difference calculation of traveltimes. Bull. Seismol. Soc. Am. 78, 2062–2076.

Wilson, T., 1965. A new class of faults and their bearing on continental drift. Nature 4995, 343–347.

Wittlinger, G., Tapponnier, P., Poupinet, G., Mei, J., Danian, S., Herquel, G., Masson, F., 1998. Tomographic evidence for localized lithospheric shear along the Altyn Tagh fault. Science 282, 74–76.

Yilmaz, O., 1987. Seismic data processing. Society of Exploration Geophysicists, Tulsa, Oklahoma.

Zak, I., 1967. The geology of Mt. Sedom. Ph.D. thesis, The Hebrew University, Jerusalem, (in Hebrew with English abstract).

Zak, I., Freund, R., 1981. Asymmetry and basin migration in the Dead Sea Rift. Tectonophysics 80, 27–38.

Zelt, C.A., Barton, P.J., 1998. 3D seismic refraction tomography: a comparison of two methods applied to data from the Faeroe Basin. J. Geophys. Res. 103, 7.187–7.210.

Zilberman, E., Amit, R., Porat, N., Enzel, Y., Avner, U., 2005. Surface ruptures induced by the devastating 1068 AD earthquake in the southern Arava valley, Dead Sea Rift, Israel. Tectonophysics 408, 79–99.